UNIVERSITY OF LEEDS

This is a repository copy of *An Ultrasound-Guided System for Autonomous Marking of Tumor Boundaries During Robot-assisted Surgery*.

White Rose Research Online URL for this paper:
https://eprints.whiterose.ac.uk/214446/

Version: Accepted Version

Article:

Marahrens, N., Jones, D. orcid.org/0000-0002-2961-8483, Murasovs, N. et al. (2 more authors) (2024) An Ultrasound-Guided System for Autonomous Marking of Tumor Boundaries During Robot-assisted Surgery. IEEE Transactions on Medical Robotics and Bionics. ISSN 2576-3202

https://doi.org/10.1109/TMRB.2024.3468397

© 2024 IEEE. Personal use of this material is permitted. Permission from IEEE must be obtained for all other uses, in any current or future media, including reprinting/republishing this material for advertising or promotional purposes, creating new collective works, for resale or redistribution to servers or lists, or reuse of any copyrighted component of this work in other works.

Reuse

Items deposited in White Rose Research Online are protected by copyright, with all rights reserved unless indicated otherwise. They may be downloaded and/or printed for private study, or other acts as permitted by national copyright laws. The publisher or other rights holders may allow further reproduction and re-use of the full text version. This is indicated by the licence information on the White Rose Research Online record for the item.

Takedown

If you consider content in White Rose Research Online to be in breach of UK law, please notify us by emailing eprints@whiterose.ac.uk including the URL of the record and the reason for the withdrawal request.

White Rose
university consortium
Universities of Leeds, Sheffield & York

eprints@whiterose.ac.uk
https://eprints.whiterose.ac.uk/

An Ultrasound-guided System for Autonomous Marking of Tumor Boundaries during Robot-assisted Surgery

Journal:	*IEEE Transactions on Medical Robotics and Bionics*
Manuscript ID	TMRB-09-23-OA-0722.R1
Manuscript Type:	Original Articles
Date Submitted by the Author:	30-Apr-2024
Complete List of Authors:	Marahrens, Nils; University of Leeds, Electrical and Electronic Engineering Jones, Dominic; University of Leeds, Electrical and Electronic Engineering Murasovs, Nikita; University of Leeds, Electrical and Electronic Engineering Biyani, Chandra; St James's University Hospital Valdastri, P.; University of Leeds Faculty of Engineering,
Keywords:	Surgical Robotics, Autonomous System, Surgical Assistance, Robotic Ultrasound
Note: The following files were submitted by the author for peer review, but cannot be converted to PDF. You must view these files (e.g. movies) online.	
Ex_Vivo_Full.mp4	

An Ultrasound-guided System for Autonomous Marking of Tumor Boundaries during Robot-assisted Surgery

Nils Marahrens[1], Dominic Jones[1], Nikita Murasovs[1], Chandra Shekhar Biyani[2] and Pietro Valdastri[1]

***Abstract*—While only a limited number of procedures have image guidance available during robotically guided surgery, they still require the surgeon to manually reference the obtained scans to their projected location on the tissue surface. While the surgeon may mark the boundaries on the organ surface via electrosurgery, the precise margin around the tumor is likely to remain variable and not guaranteed before a pathological analysis. This paper presents a first attempt to autonomously extract and mark tumor boundaries with a specified margin on the tissue surface. It presents a first concept for tool-tissue interaction control via Inertial Measurement Unit (IMU) sensor fusion and contact detection from the electrical signals of the Electrosurgical Unit (ESU), requiring no force sensing. We develop and assess our approach on Ultrasound (US) phantoms with anatomical surface geometries, comparing different strategies for projecting the tumor onto the surface and assessing its accuracy in repeated trials. Finally, we demonstrate the feasibility of translating the approach to an ex-vivo porcine liver. We are able to achieve mean true positive rates above 0.84 and false detection rates below 0.12 compared to a tracked reference for each calculation and execution of the marking trajectory for dummy and ex-vivo experiments.**

***Index Terms*—Robotic Surgery, Autonomous System, Surgical Assistance, Robotic Ultrasound**

I. INTRODUCTION

THe most crucial element in resecting a tumor is isolating the entirety of cancerous tissue while sparing as much healthy tissue around it as possible. Therefore, pre-operative imaging is regularly used in assessing the intervention's necessity, its treatment plan and projected outcomes. Without intra-operative imaging, the surgeon must spatially map knowledge extracted from the pre-operative images to the scene they perceive during surgery. In open procedures, the surgeon may rely on their tactile abilities to assess the tumor location and boundries more accurately. Additionally, intra-operative imaging, most commonly US, may be used as a real-time tool for verification during surgery. In Minimally Invasive Surgery (MIS) on the other hand, the physical separation and resulting absence of haptic feedback between the surgeon and the surgical site renders full tactile interaction impossible.

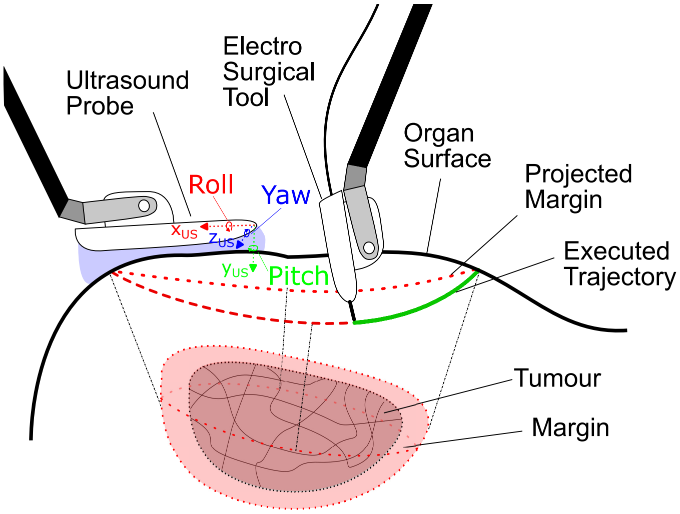

Fig. 1: Concept overview: The internal tumor geometry is captured via US, projected onto the surface and eventually marked via an electrosurgical tool.

US may present a possible solution for intra-operative tumor localization. Despite the existence of 3D US probes, they are still largely used with single-line arrays, leading to 2D slices of the target regions. Regarding intra-operative US imaging, manual and robotic laparoscopy require specific US systems, encapsulating miniaturised US probes exclusively available as 2D (B-Mode) US probes. While these systems can potentially reduce the perceptual gap, they may require extensive training before they can be accurately used by the surgeon [1]. An additional challenge may be the spatial mapping of the US scan from the probe to the endoscopic video scene and then further onto the actuating instrument to guide the resection. To do so, it is common for surgeons to mark the projected boundaries of the tumor onto the organ surface via electrosurgical tools, e.g. after temporary highlighting via Indocyanine Green (ICG) [2], [3]. A concept in imaging skins has been proposed to highlight radioisotopes injected into the bloodstream [4], potentially enabling Augmented Reality (AR) overlays with preoperative information. The surgeon's knowledge of the probe's 3D location and the US scan's location is imprecise, but robotic systems could excel in reaching specific, predefined locations through an US scan. This paper presents a first autonomous tumor boundary extraction and marking concept using IMU sensor fusion and contact detection from the electrical signals of an ESU, requiring no force sensing.

*This work was supported by the Royal Society, by the Engineering and Physical Sciences Research Council (EPSRC) under grant number EP/R045291/1, and by the European Research Council (ERC) under the European Union's Horizon 2020 research and innovation program (grant agreement No 818045).

[1] Nils Marahrens, Dominic Jones and Pietro Valdastri are Storm Lab U.K., School of Electronic and Electrical Engineering, University of Leeds, Leeds, UK (`elnma@leeds.ac.uk; d.p.jones@leeds.ac.uk; elnmur@leeds.ac.uk; p.valdastri@leeds.ac.uk`)

[2] Department for Urology, James's University Hospital, Leeds Teachings Hospitals NHS Trust, Leeds, UK (`c.s.biyani@leeds.ac.uk`)

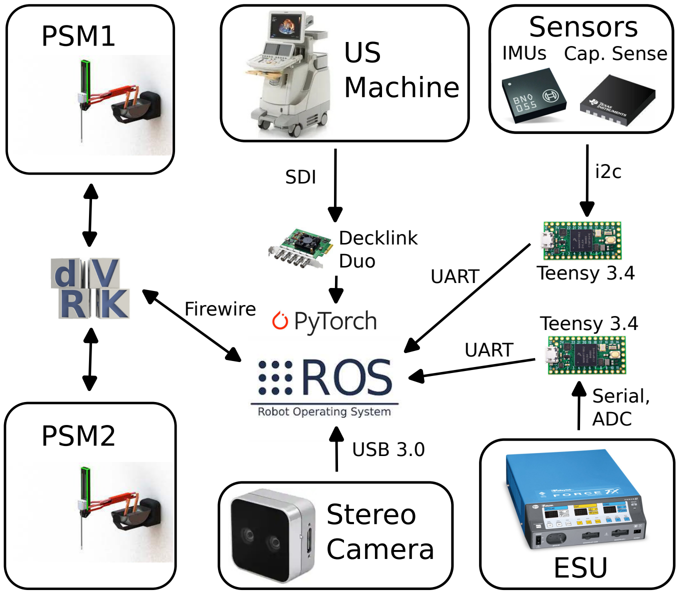

Fig. 2: ROS-embedded system structure showing hardware and software components as well as their interfaces for data interchange.

II. State of the Art

A. Current Intra-operative Imaging Guidance Techniques

Determining and referencing a target location inside the patient may, in theory, be done via pre- or intra-operative imaging or conceivably a combination of the two.

Soft tissue registration is a major bottleneck in referencing pre-operative data, allowing pre-operative imaging data to be registered to the surgical scene is challenging while being investigated for various surgical applications [**?**]. While this may work relatively well for specific, more constrained, and potentially more rigid organs such as the prostate [6], this is not generally the case, particularly for large, soft and loosely constrained organs such as the liver. In these cases, the deformation between the pre-operative image data acquisition and the intra-operative registration process may be substantial [7]. While works on more constraint organs such as the heart [9] or the brain [8] have reported errors as low as $2.5mm$ or $1.7mm$, this is may not be achievable with highly mobile and flexible organs such as the liver. Some recent works have evaluated approaches on ex-vivo liver, observing a root mean square error of $7.9mm$ [10].

Therefore, research in robotically assisted surgery has primarily focused on intra-operative methods, specifically US. Intra-operative US may be applied in three ways: extracorporeally, endoluminally or intracorporeally. Extracorporeal US is a well-researched area, including robotic guidance and its potential usage with surgical robotics [11], [12]. The main issue is limited resolution of these systems, as larger penetration requires lower frequencies and integration into the patient's spatially constrained environment, further requiring spatial co-registration. Endoluminal probes, such as Transrectal Ultrasound (TRUS), have been shown to work well in conjunction with robotic systems and can be registered to the surgical robot via the tissue boundary [13]. However, they are limited to a few target regions close to natural orifices or their attached tubular organs. Lastly, the most commonly used solution is intracorporeal US probes, predominantly in the form of a pick-up probe [14] that have also found their way into the commercial market. In the following, we shall therefore focus on intracorporeal US.

B. Automated and Assisted Resection

Automation and autonomous surgical assistance are increasingly relevant areas of research, with applications ranging from automated suturing to autonomous endoscope guidance [31]. Research on robotic surgery's automation of tumor resection primarily focuses on improved scan acquisition and visualization, as well as automated resection in general, not necessarily with intra-operative imaging as a means of verification.

Concerning US, previous works have investigated improving the visualization by projecting the current 2D US image into the probe visible in the endoscopic scene, viewed by the surgeon in the console [16]. This work involves an optical marker attached to the intracorporeal US probe to extract the current tool pose for subsequent scan projection into the scene. While this provides a momentary slice, it does not provide assistance in reconstructing the 3D anatomical structure.

Our previous works [17] along with [14], have looked at autonomous US scan acquisition of blood vessels, their 3D reconstruction, and accuracy in robotic surgical scenarios. Additionally, [18] has looked at newer da Vinci robot versions and compared their accuracy. However, these results are not directly transferable since the accuracy is measured in unloaded conditions. The system's accuracy under loading such as an US probe or applied contact with the tissue surface, will cause clear deviations from these results.

Several approaches have been proposed to enable automated assistance of cutting and resection of tissues. Previous work has focused mainly on specific subtasks, such as tissue stretching [19] via FEM simulation and reinforcement learning or automation via custom-built pick-up tools on a highly abstracted planar tissue phantom [20].

While these approaches assist in automating resection, they may not provide improved resection results, as they do not reference the tumor beneath the surface.

Recently, [21] demonstrated fully autonomous large bowel anastomosis. While the application is quite different to the one intended in this work, it further shows the extensive additional setup necessary to reference tissue and anatomical stuctures to perform autonomous assistenace. The system heavily relies on previously injected optical markers containing toxic ICG and Cyanoacrylate. Furthermore, it is unclear how the results, performed on bowel tissue, could be used for improved tumor resection as they lie below the tissue surface. Work by the same group has further focused on autonomous electrosurgery, enabling linear cuts on planar surfaces [22], [23]. Similar to the group's previous work in [21], the system relies on injected markers and is built on a proprietary platform rather than a full surgical robotic system.

Research on using reconstructed scan geometries to autonomously perform or assist during tumor resection has been limited, combining resection and intra-operative imaging. To date, only a single work has more deeply looked into automated tumor resection via intracorporeal imaging. Pratt et al. demonstrate autonomous cutting on a planar phantom [24]. Custom visual markers are used to track the US probe and a high-velocity water jet to perform tissue cutting based on the US image. The system was tested in a benchtop trial using a custom-designed PVA cryogel phantom and was found to be capable of dissecting a modelled tumor at a margin with a mean difference of $0.77mm$ between desired and visually measured margins over multiple experiment runs. While this approach does include US guidance, the experiments are limited to a simple planar phantom with a curved, linear contour. The work still incorporates optical markers in the images, while the endoscopic camera remains static throughout the experiments. It uses a water jet instead of standard tools that directly interact with the surface to avoid tissue ablation.

C. Contributions

This work aims at realising a comprehensive approach to assisting during tumor resection and implementing the first steps towards fully autonomous execution, thereby providing means for improved results with smaller tumor margins. It is the first work to attempt this with a non-planar surface geometry in an intracorporeal, surgical robotic setting. Contrary to previous work, our method employs standard electrosurgery and requires no visual feedback aside from the initially extracted surface point cloud, in particular, no extensive visual tracking of the tool position over time. Finally, a comprehensive analysis is carried out to assess the accuracy of the approach. Finally, the approach's accuracy is assessed through a comprehensive analysis on a controlled, replicable environment and in ex-vivo tissue, marking the first of its kind in intracorporeal US scanning. An overview over the system is depicted in Figure 1.

III. MATERIALS AND METHODS

In the following, we will outline the several components and developed concepts for their realisation. See Figure 2 for a visual overview of the system's components and interfaces, along with Figure 4 showing the algorithmic pipeline. The nomenclature used throughout this and the following sections is defined in Appendix VIII.

A. Robotic Setup

To enable US-guided tumor boundary marking, we developed a platform, based around two Patient Side Manipulator (PSM), providing integration into Robot Operating System (ROS). This platform has become the gold standard for research on robotic surgery over the past 20 years [25]. For all experiments, we used da Vinci Research Kit (dVRK) version 2.1 and calibrated all the arms using the integrated routines. This included the novel calibration of the third joint that was recently added to the dVRK software stack. To ensure both robots have the same base frame, we placed the entire setup on a levelled vibration isolated optical table (Newport RS2000, Newport Corporation, Irvine, CA, USA). Additionally, we integrated four Optitrack Primex 13 Infrared (IR) tracking cameras (NaturalPoint, Inc., Corvallis, OR, USA) and IR markers to enable the acquisition of ground truth data. We further used these markers to ensure both PSM frames were aligned with each other as well as the levelled tabletop for calibration, a point that still remains largely unaddressed within the dVRK framework and community [26].

The initial aim was to provide assistance using only standard da Vinci monopolar tools. However, we found this to be hardly feasible with consistent accuracy. While the instruments are made of rigid components, they are inherently compliant due the tendon-driven design of the robot. Consequently, they experience significant backlash, allowing for only very imprecise inference of the tooltip pose and causing a degradation in the precision of the marked shapes in preliminary testing. To increase the precision, we designed a pick-up device that includes an IMU for improved pose measurement, important for 3D US scan reconstruction, probe control control as well as important for marking the tissue surface despite contact forces. Previous works on tissue cutting have chosen a similar approach to integrate novel tools into the da Vinci via pick-up devices [20], [27]. As robotic end-effector tools, we employed standard da Vinci instruments: a Fenestrated Bipolar Forceps for engangement with any pick-up devices and a Large Needle Driver for fiducial registration on each of the two arms. Additionally, a pick-up device enabled the integration of an IR tracker, which was crucial for assessing the system's accuracy in marking the tumor projection; however, it was not used in the actual deployment of the final system. Similarly, the US probe is designed as a pick-up device with an integrated IMU, the details of which can be found in [17].

B. IMU sensor fusion scheme

We developed an algorithm for fusing IMU measurements with measured robot kinematics to improve the kinematic accuracy and precision regardless of contact forces. Using the Mahony filter [28], we can calculate the update of $\mathbf{\Delta\omega_{US}}^{US,fused}$ based on the direction of gravity (aligning with $\mathbf{z}_{PSM}$) as follows

$$\Delta\omega_{US}^{US,fused} = \mathbf{z}_{US}^{PSM} \times \frac{\mathbf{g}_{US}}{\|\mathbf{g}_{US}\|} \tag{1}$$

and then updating the T_{US} in quaternion space via

$$\Delta\mathbf{q}_{US}^{US,fused} = \frac{1}{2}\mathbf{q}_{PSM}^{US} \otimes \left(0, \Delta\omega_{US}^{US,fused}\right) \tag{2}$$

$$\mathbf{q}_{PSM}^{US,fused} = \frac{\mathbf{q}_{PSM}^{US} + \Delta\mathbf{q}_{US}^{US,fused}}{\|\mathbf{q}_{PSM}^{US} + \Delta\mathbf{q}_{US}^{US,fused}\|} \tag{3}$$

where $\otimes$ is the quaternion product. Note that this is equivalent to our previous work [17]. Next, we further update the position of the end-effector based on the newly calculated

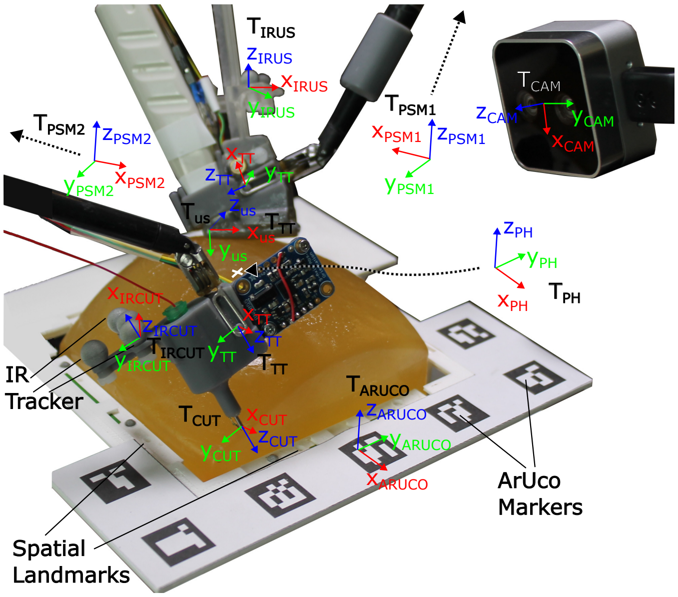

Fig. 3: Overview of setup and frames used. T_{PSM1} and T_{PSM2} sit at the fulcrum point of each PSM, while T_{PH} is located at the center of the US phantom. T_{CUT} and T_{US} are the tooltip frame for the marking tool and US probe respectively, along with the tool-attached IR tracking frames T_{IRCUT} and T_{IRUS}.

orientation. For this, we assume that the first three joints of the robot are relatively accurate. The motivation for this is the fact that the first two degrees of freedom (azimuth and polar angle around the fulcrum point) are actuated in close proximity to the motor, reducing tendon length and thus complex tendon elasticity and friction. The third degree of freedom (tool insertion), in turn, is actuated by a longer tendon but sits before the coupling plate with the instrument. Since this joint, however, has no influence on the orientation of the tool tip, it will not appear in the IMU's orientational measurement. Therefore, we now propose a scheme to update only the last three joints of the robot, on the robotic tool.

Based on the results of equation 3, the transformation of the last three joints is calculated as

$$\mathbf{R}_{l4}^{tt,fused} = (\mathbf{R}_{PSM}^{l4})^{-1}\mathbf{R}_{PSM}^{tt,fused} \tag{4}$$

Subsequently, this rotation's Euler angles (ZYX rotation order) are calculated. The Euler angles are set up specifically to match the three joint angles at the tip of the robotic instrument

$$\theta_{l4-l6,fused} = \begin{bmatrix} \arctan(r_{2,1}, r_{1,1}), \\ \arctan(-r_{3,1}, \sqrt{1-(r_{3,1})^2}), \\ \arctan(r_{3,1}, r_{3,3}) \end{bmatrix} \tag{5}$$

where $r_{i,j}$ is the element in column i and row j of $R_{l4}^{tt,fused}$. Lastly, the three fused joint angles replace the originally measured joint angles from the kinematics in the following manner

$$\mathbf{q}_{fused} = \left[\theta_{l1}, \theta_{l2}, \theta_{l3}, \theta_{l4,fused}, \theta_{l5,fused}, \theta_{l6,fused}\right] \tag{6}$$

where θ_{l1} to θ_{l3} are the joint angles of the first three joints, directly obtained from the robot joint measurements, and $\theta_{l4,fused}$ to $\theta_{l6,fused}$ are the fused joint angles from the previously presented update rule. Plugging these newly obtained, fused joint angles into the direct kinematics equations

$$\mathbf{x} = f(\theta_{fused}) \tag{7}$$

to obtain the updated forward kinematics pose (tooltip position and rotation) from the updated joint angles. The updated position allows us to account for the PSMs mechanical play and compliant design, enabling more precise US scans.

C. Arm Co-Registration

Arm co-registration is a major challenge in collaborative applications on the dVRK platform. Normally, the PSMs sit on a patient cart that structurally connects the two robots. Each PSM can be moved via a passive kinematic chain, often referred to as the SetUp Joints (SUJ). While the joint angle along this chain is equipped with encoders and can thus be measured, the measurements on the first-generation da Vinci systems are known to be imprecise. These errors are further exacerbated by a relatively long kinematic chain.

The dVRK Wiki states that the recently introduced SUJ controllers that allow extracting the SUJ encoder measurements, only achieve an accuracy of $\pm 5cm$ [29]. This is more than an order of magnitude higher than that of the active part. While some approaches, such as [30], externally track the SUJs, another common option is to co-register different arms via spatial landmarks, further allowing them to be easily transferred to a lab bench setup.

Please note that this may not be necessary for more modern versions of the da Vinci, such as the Xi, which possess a completely redesigned patient cart and passive SUJ, achieving submilieter accuracy in their unloaded state [18]. These, however, do not yet have an open-sourced API that allows their control, although the da Vinci S and Si are planned to be more widely integrated into the dVRK framework in the upcoming years and eventually replace the current dVRK using the first-generation da Vinci robotic system. Note that the work including IMU sensor fusion may be still be useful even with more novel platforms as they can account for deflections due to external forces as they are present during scanning and surface marking.

To enable arm co-registration, we resorted to touching spatial landmarks on 3D printed frames with the robotic tooltips. We placed the landmarks in a way that allowed for direct calculation of the predefined axes of the phantom frame e.g. the connecting vector between two landmarks always resulted in a $\mathbf{T}_{PH}$ axis (see $\mathbf{T}_{PH}$ in Fig. 3). We then took the mean over all calculated axes and adjusted both axes to result in perpendicular axes. We then calculated the origin by minimising the squared error for all landmarks via the following formula

$$\mathbf{p}_{PSMi}^{REF} = \frac{1}{n}\sum_{j=0}^{n}(\mathbf{p}_{PSMi}^{(j)} - \mathbf{R}_{PSMi}^{REF}\mathbf{p}_{REF}^{(j)}) \tag{8}$$

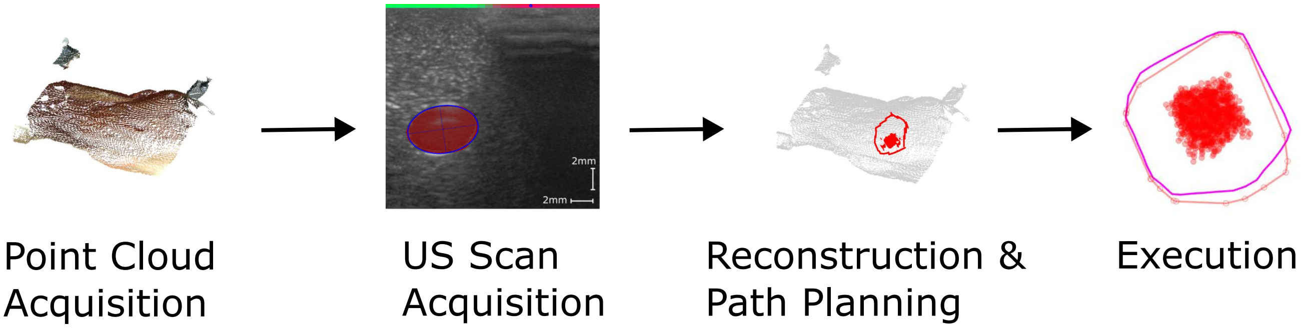

Fig. 4: Overview over the algorithmic pipeline: 1) A surface point cloud is extracted from the real sense and referenced to the robot via ArUco markers 2) Based on the surface information, a scan is acquired 3) The 3D geometry is projected onto the surface using one of the two suggested methods 4) The planned path is executed on a second robotic arm

Where $\mathbf{p}_{PSMi}$ is the landmark position as measured by the robot in its own frame, $\mathbf{p}_{PH}$ is the landmark position in $\mathbf{T}_{PH}$ as known from the design of the phantom frame and $\mathbf{R}_{PSMi}^{REF}$ is the rotation between frames $\mathbf{T}_{PH}$ and $\mathbf{T}_{PSMi}$ as previously obtained.

In total, we achieve a fiducial registration error of $0.65 \pm 0.21mm$.

D. 3D surface point cloud registration

While position, pitch, and yaw can all be determined through the US image, this is not the case for the roll angle (see Figure 1 for roll, pitch, and yaw correspondence). Adapting the roll angle usually requires knowing the surface normals to move the probe tangentially to the surface. This can be achieved via a stereo camera that visually estimates the surface normals. This is a common approach in extracorporeal US. Previous works have already used this information to automate specific tasks, such as tissue retraction [31].

We extracted the surface geometry using a stereo camera (Intel Realsense 405d, Intel Corporation, Santa Clara, CA, USA), analogous to a stereo endoscope. The camera was placed at a distance of roughly $13cm$ from the surface to account for the larger lens disparity compared to an endoscope. The average point distance was downsampled to $3mm$ for the phantom surface to filter outliers, and the closest point on the surface was found by interpolation. To calculate the surface normal, we performed Principle Component Analysis (PCA) of all points within a $10mm$ radius around the found point using VTK (Visualization Tool Kit (VTK), Kitware Inc., Clifton Park, NY, USA). For hand-eye calibration, we employed ArUco markers attached to the 3D-printed frame used for IR tracking and arm co-registration. Using the mesh from the phantom mold CAD model as ground truth, we calculated the mean angle error of the normal vectors extracted from the point cloud to be around $4.63°$ with a maximum error of $16.95°$ that was mainly observed on the edges of the phantom. The mean and root mean square errors were $0.16mm$ and $0.91mm$, respectively.

E. Modified Electrosurgical Unit

For autonomous marking, we employed a commercially available ESU (Valleylab Force FX-8, Medtronic plc, Minneapolis, MN, USA). The system includes two DB-15HD ports at the back capable of providing real-time data from the system. To use this data, we fed the signals from both ports into a Teensy 3.6 that processed the data and then published it into the ROS environment (see Figure 2).

Since the dVRK does not offer reliable force estimation, further measures are needed to ensure proper contact of the tooltip with the tissue surface. Previous research has already looked at using the da Vinci tools to estimate tissue impedance [32]. Similarly, the impedance of the instrument changes once contact with the tissue surface is established. While the ESU's internal controller will try to reach target values for current and voltage, it might not always be feasible; if there is no contact with the tissue surface, a voltage difference can be created, but the current flow will be prohibited. Consequently, the power output P_{out} will vary

$$P_{out} = U \cdot I \tag{9}$$

where U and I are the measured voltage and current, respectively.

The goal is to apply as little force to the surface as necessary but establish enough contact to maintain a clean mark. In order to control the instrument, we observe the output over the desired power ratio

$$r_P = \frac{P_{out}}{P_{des}} \tag{10}$$

When contact is lost, the average achievable power will be significantly lower. Figure 5 shows the ratio over different desired output power settings. This is an observation that we will use to control the probe. To adjust the contact, we lifted off the probe until contact was lost before reapproaching the surface until contact was restored.

F. US tumor Scan

For detecting features in the US image, we trained a standard U-Net [33] in PyTorch to segment out feature-dense regions.

Fig. 5: Difference between measured voltages and current between contact and no contact over desired power settings.

Additionally, we employed a custom-built deep neural network to estimate the coupling quality between the US probe and the tissue surface based on the US image. The details of these can be found in our previous work on autonomous vessel navigation [17]. We use a Philips L15-7io probe driven by a Philips iU22 US machine (Philips, Amsterdam, NL). To ensure the probe is not applying excessive pressure, we let the robot slightly lift off the probe as it moves. As soon as the probe detaches from the tissue surface, the contact detection sets in and slightly adjusts the probe position towards the surface. In this manner, we can autonomously scan without requiring an additional force sensor, unlike our previous publication [17].

Initially, we assume the probe starts at a location in the approximate vicinity of the tumor and propagates along the image normal axis, also commonly referred to as elevation direction. Once a tumor is detected, it is centered in the image while continuing to move in the image normal direction. Once the probe has passed the tumor, the current centroid of the point cloud is calculated and used to determine the center of rotation on the tissue surface. Subsequently, the probe is rotated by 30° and propagated back towards and across the tumor. Lastly, this is repeated a second time with a 60° angle compared to the initial position. We found that for the phantom tissue three scans were necessary to capture the full 3D geometry despite varying contact quality that was used as a control measure. Rotation angles 30° and 60° were chosen to allow for varying angles while reducing the risk of the robot running into joint limits. Note that for ex-vivo experiments, we only relied on a single scan as tissue movement caused significant differences between the scans, while we did not observe contact quality changes to the same degree as we did with the phantoms.

G. Trajectory Generation

According to surgeon feedback, there is no standardised way to project the internal 3D tumor geometry onto the surface. We suggest that this will depend on the eventual goal of the resection. If the goal is to resect a liver segment or lobe, a direct upward projection with the same vector for every point may be desirable (Direct Point Projection (DPP)). This, however, may not be practical for an actual resection since a cylindrical cut-out is usually not feasible. In these cases, it may be desirable to project the internal geometry to its closest point on the surface (Closest Point Projection (CPP)). This may be seen as a simple representation of the commonly seen wedge-shaped tissue extraction for simplified reconstruction. The difference between the two methods becomes further exacerbated depending on the surface structure. In the following, we will assume the surface to be either planar or convex since this primarily reflects the general surface structures metabolic organs such as the liver or kidney. While for a planar surface, the two projection methods might be almost identical, this may not be the case if the shape of the surface is convex. In these cases, the CPP will result in a larger projected area. The difference between the two methods is further depicted in Figure 6. Furthermore, the formulas used for plane projection are defined in Appendix IX.

To marginalise the tumor, we first find its outer surface. In the following, we assume that we are dealing with a relatively round tumor without major concave surface regions. In this case, finding the outer surface reduces to finding the convex hull, for whose calculation numerous methods exist. The convex hull of A, referred to as $\{A_{CV}\}$, is the smallest convex set of points that encloses all of the points in A. For calculating the convex hull, we employ the Quickhull algorithm provided by Scipy [34]. Once the set of points $\mathbf{p}_i^{(A_{CV})}$ of the convex hull $\{A_{CV}\}$ is found, we determine the centroid $\mathbf{p}_c^{(A_{CV})}$ of the resulting surface. We then calculate the normal vector pointing away from the contour for each convex hull point. We achieve this by considering the vector connecting the centroid to each convex hull point. Since we know the centroid needs to lie within the contour, it can be expressed as a linear combination of the surface tangent and normal at that point. We thus define the connecting vector from the centroid to point i of the convex hull as

$$\mathbf{v}_{c,i}^{(A_{CV})} = \mathbf{p}_i^{(A_{CV})} - \mathbf{p}_c^{(A_{CV})} \tag{11}$$

We further guarantee with this method that the fraction in the normal vector direction always points outward, away from the contour. We start by calculating the two tangent vectors $\mathbf{t}^{j,0}$ and $\mathbf{t}^{j,1}$ of each simplex that point $\mathbf{p}_i^{(A_{CV})}$ is part of

$$\mathbf{t}_{j,k}^{(s_j)} = \frac{(\mathbf{p}_{k+1}^{(s_j)} - \mathbf{p}_k^{(s_j)})}{\|\mathbf{p}_{k+1}^{(s_j)} - \mathbf{p}_k^{(s_j)}\|} \tag{12}$$

where $k = \{0, 1\}$ and $\mathbf{p}_k^{(s_j)}$ is the k^{th} point of simplex s_j. This leads to a simplex normal $\mathbf{n}_{i,k}^{(s_j)}$ at point i via the following formula

$$\mathbf{n}_{j,k}^{(s_j)} = \mathbf{v}_{c,i}^{(A_{CV})} + \mathbf{t}_{j,k}^{(s_j)} \left(\left(\mathbf{t}_{j,k}^{(s_j)} \right)^T \mathbf{v}_{c,i}^{(A_{CV})} \right) \tag{13}$$

The normal $\mathbf{n}_i$ for each point is then inferred by calculating the average over-all simplex face normal. Finally, the set of

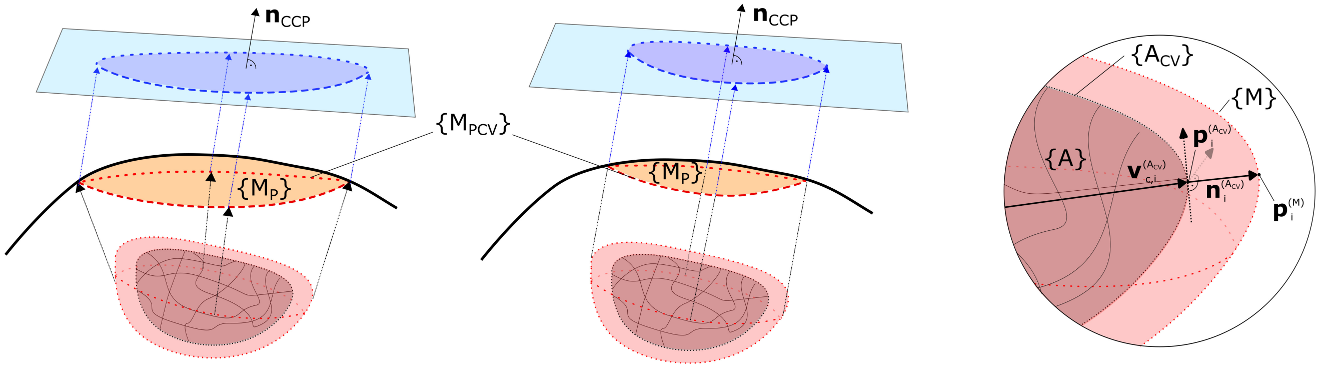

Fig. 6: Comparison between different projection methods. Left: CPP using the closest point as surface projection.Center: DPP using the same vector to project each point to the surface. $\mathbf{n}_{CCP}$ marks the surface normal plane at the surface point closest to the centroid of the tumor. A clear difference can be observed in the size of the different projections both on the surface marked as red contours $\{M_{PCV}\}$, as well as on the projected outline on $\mathbf{n}_{CCP}$ plane. Right: Zoomed in view showing the different point sets and vector quantities involved in the calculation of the margin, in particular the surface normal $\mathbf{n}_i^{(A_{CV})}$ and surface point $\mathbf{p}_i^{(A_{CV})}$.

points $\{M\} = \mathbf{p}_i^{(M)}$ defining the margin is calculated by updating each point with its scaled surface normal vector

$$\mathbf{p}_i^{(M)} = \mathbf{p}_i^{(A_{CV})} + d_m \mathbf{n}_i^{(A_{CV})} \tag{14}$$

with d_m being the desired margin.

To infer the trajectory on the surface, we project all points in $\{M\}$ up onto the surface using one of the previously outlined methods, resulting in $\{M_P\}$. Next, we need to identify all points on the outer edge of the projected points. For this, we further project all points $\{\mathbf{p}_i^{(M_P)}\}$ onto the surface normal plane at the point closest to the centroid P_c. In the planar projection, we then determine all points in $\{M_P\}$ that are part of the convex hull in the planar projection, resulting in the final set of points $\{M_{PCV}\}$ making up the surface trajectory. This process is further depicted in Figure 6.

H. Marking Tool Control Scheme

While the IMU on the US probe is predominantly used to determine the correct location of the US scan, the IMU on the marking tool feeds back into a controller to adjust the probe location. For this, we implemented a Proportional Integral (PI)-controller that provides an updated cartesian position to the dVRK software framework in the form

$$\mathbf{x}_{ctrl,i+1} = \mathbf{x}_{des,i} + \mathbf{K}_p \Delta\mathbf{x}_{des,i} + \mathbf{K}_i \sum_{k=0}^{k=i+1} \Delta\mathbf{x}_{des,k} \tag{15}$$

where $\mathbf{x}_{ctrl,i}$ describes the six-dimensional vector composed of 3D location, roll, pitch, and yaw angles at the i^{th} time step and $\mathbf{x}_{des,i}$ describes the difference between desired and current pose. $\mathbf{K_p}$ and $\mathbf{K_i}$, in turn, are diagonal matrices defining the gains for updating the components of $\Delta\mathbf{x}_{ctrl,i}$. We start each trajectory by moving the end-effector at a safe distance of $10mm$ from the surface. We then initialise the controller by slowly adapting $\Delta\mathbf{x}_{ctrl,i}$ along with the end effector pose until root squared error for position and orientation are below $0.75mm$ and $0.25°$, respectively. After that, we start approaching the tissue surface until a contact is detected. We then start moving along the trajectory on the surface. During the following, we gradually and slightly lift the probe off the surface. After a $3mm$ ($10mm$ for ex-vivo) distance, we adapt the contact. For this, we lift the probe off the surface until the contact is lost, if necessary, and then re-approach it. This way, we achieve a saw-tooth motion that prevents the marking tool from getting stuck inside the tissue and minimises contact forces. Since we are only interested in marking the surface, ensuring contact every $3mm$ is sufficient to outline the contour, as the ESU will also mark the tissue surface if slightly above the surface.

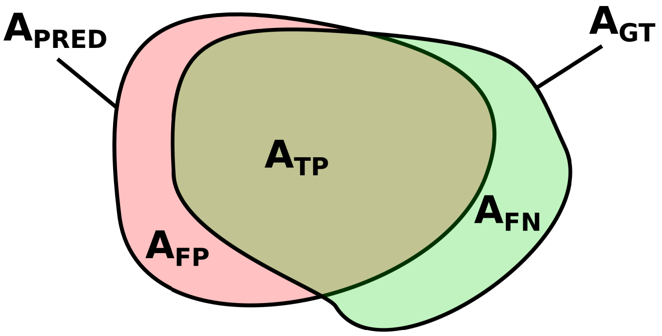

Fig. 7: Different areas used in the calculation of metrics.

I. Metrics

To compare the different scans on the tissue surface, we project all results, both IR-tracked and inferred, into the same tangential plane. Using the ground truth mesh, we chose the tangential plane at the point closest to the IR-tracked centroid.

For the assessment of the projections in this plane, we consider the True Positive Rate (TPR) (sensitivity) r_{TP} or,

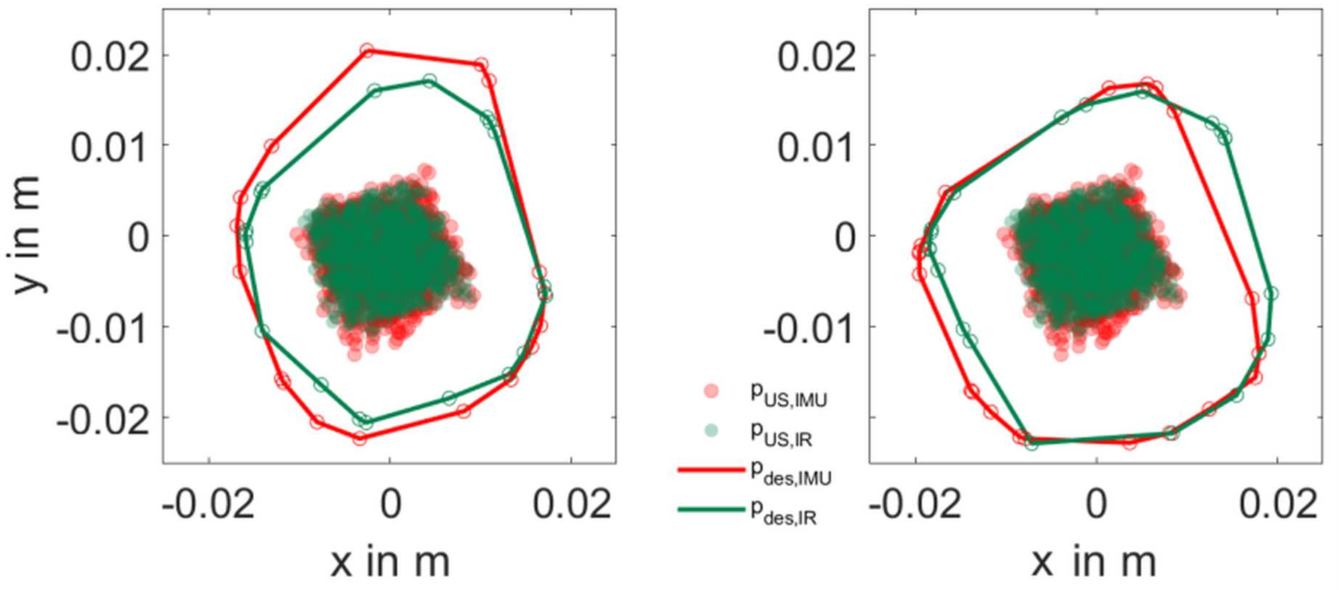

Fig. 8: Point clouds showing the projected scan along with outline of the trajectories resulting from direct projection (**left**) and closest point projection (**right**) and for IR-tracked (red) and IMU-fused kinematics (green)

equivalently, the False Negative Rate (FNR) $r_{FN} = 1 - r_{TP}$, also known as miss rate, as well as the False Discovery Rate (FDR) r_{FD}. Based on the areas outlined in Figure 7, they are defined as follows:

$$r_{TP} = \frac{A_{PRED} \cup A_{GT}}{A_{GT}} = \frac{A_{TP}}{A_{GT}} = 1 - r_{FN} \tag{16}$$

$$r_{FD} = \frac{A_{GT} - A_{TP}}{A_{GT}} = \frac{A_{FP}}{A_{GT}} \tag{17}$$

J. US phantom design

In order to develop and assess the system under controllable conditions, we designed an ultrasound phantom, keeping in mind a final application. For the design and subsequent experiments, we made the following assumptions: (1) tumor masses are relatively small in diameter ($d < 20mm$), such as very early-stage Hepatocellular carcinoma (HCC) [35]. We also assume the tumors to be (2) relatively round and (3) lie closely below the surface (starting around $5 - 10mm$ from the organ surface). The last assumption is necessary for a minimally invasive resection to make more sense than performing a full lobectomy. As target margin we chose $7.5mm$, roughly half the tumors diameter. This is slightly smaller than the suggested minimum $10mm$ safe margin from literature [**?**], [36], [38]. By choosing a smaller margin be may better capture the inaccuracies in our target measures TPR, FNR and FDR.

To provide a realistic chance of translating results from the lab bench to an ex-vivo organ, we extracted the curved surface geometry of a CT liver scan, which we integrated into a mold with a support surface of $95 \times 95mm$. The gelatin-water ratio was chosen to make the tissue phantom as soft as possible while maintaining US-properties close to those of real tissue. The precise phantom composition is attached in Appendix VII. The used phantom is further shown in Figure 3. For the tumor masses, we chose $15 - 18mm$ hydrated Polyacrylamide (PAM) beads that, due to their acoustic properties relative to the gelatine, make them appear as dark areas in the US slices.Unfortunately, we noted that, presumably due to the applied heat during phantom production, the masses' diameter was reduced by $2 - 3mm$.

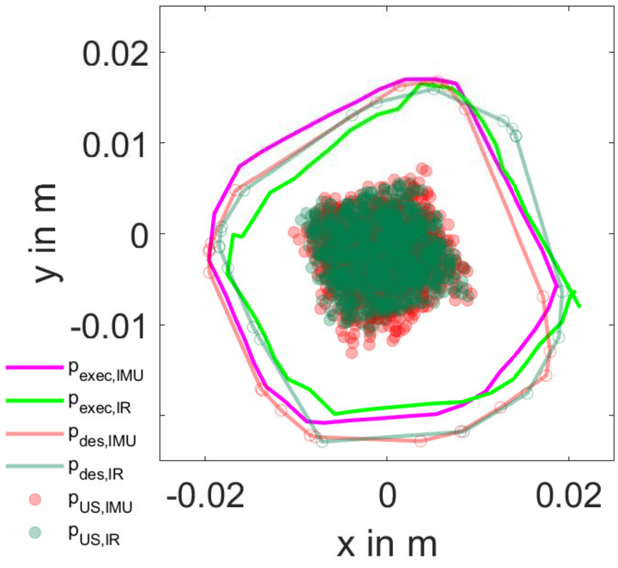

Fig. 9: Point clouds showing the projected scan along with outline of the trajectory resulting from closest point projection, along with the executed trajectory measured by IMU-fused kinematics $\mathbf{p}_{exec,IMU}$ and by IR tracking $\mathbf{p}_{exec,IR}$.

IV. EXPERIMENTAL VALIDATION

To scrutinise the developed approach, we carried out experiments of increasing complexity. First, we let the system perform autonomous scans on a tumor phantom, allowing a comparison of the results against a ground truth surface and creating a controlled environment for an in-depth assessment of the system's accuracy. Eventually, we translated the approach onto an ex-vivo liver sample for initial conclusions about its feasibility under more realistic circumstances.

A. Phantom Trajectory Generation

We cast three phantoms with identical surfaces and placed a single mass in each, varying its locations. We placed the masses as far apart from each other as possible to cover a wider range of scenarios and surface topologies. As a consequence on mass lay close to the peak of the convex surface, while other two masses were at lower points close to the surface and on opposite sides of the phantom. We ran five repetitions on each of the three masses, making 15 distinct scans, and calculated the trajectory for further evaluation. To begin with, the probe was set at a random location around the tumor, before the scanning procedure was run as outlined in Section III-F. Once the scans were acquired, the results were processed, calculating the direct and closest point projections. The results of the 15 scans are outlined in Table I. The TPR for both methods lies around 0.9, slightly above these values for CPP and slightly below for DPP. Similarly, the FDR for both methods is comparable, yet slightly lower for the CPP. Furthermore, the mean standard deviation of all runs is again slightly lower for the closest point method. We assume the higher robustness may be explained by the fact that the projection vector is calculated individually for each point rather than based on a single estimate of the connecting vector between the mass centroid and its closest point. Examplary results for both projection methods are shown in Figure 8.

TABLE I: True Positive Rate, False Discovery Rate and False Negative Rate for the two different projection methods: DPP and CPP. Note that results for r_{FD} are complements of r_{TP} ($r_{FD} = 1 - r_{TP}$).

Method	r_{TP}	r_{FD}	r_{FN}
DPP	0.879 ± 0.059	0.151 ± 0.088	0.121 ± 0.059
CPP	$\mathbf{0.907 \pm 0.036}$	$\mathbf{0.148 \pm 0.060}$	$\mathbf{0.093 \pm 0.036}$

When comparing the 3D scans, we found the average distance between the projected scan centroids to be $3.2 \pm 1.4mm$. This is coherent with the results since the shift also accounts for roughly 10% of the radius of the margined mass ($15mm$ diameter plus twice the $7.5mm$ margins). Similarly, we get a 10% reduction in the TPR. While this error is likely caused by the inaccurate kinematics of the PSM, even after IMU fusion, another potential source of error might be the grid size of the extracted point cloud. Currently, this is limited to a grid of $3mm$ average distance, which is used for closest point interpolation.

Comparing the inferred trajectory against the convex hull of an unmargined tumor, we find an overlap of 0.992. Only in two cases did the convex hull slightly cross the ground truth tumor outline. Since we do not expect the inaccuracies to scale up with margin size, we would expect this to vanish for a larger margins.

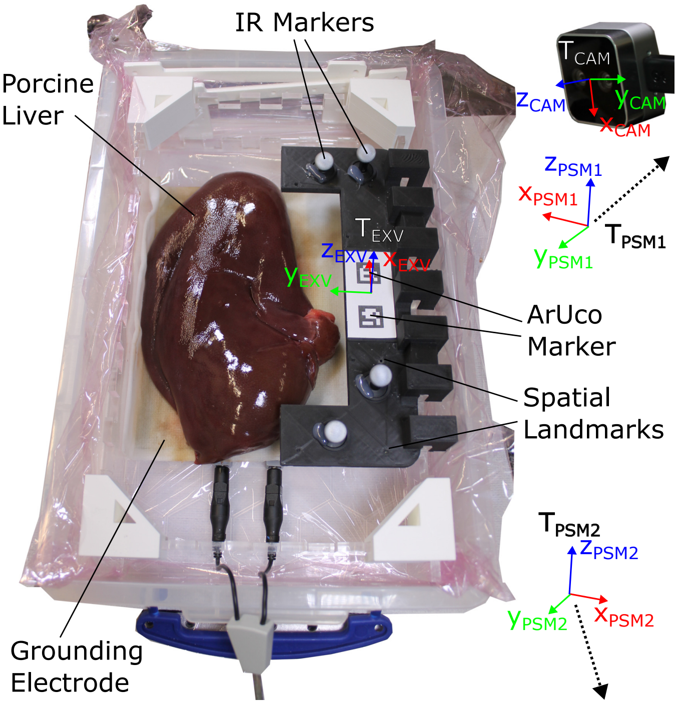

Fig. 10: Experimental setup for ex-vivo trials, including frame with ArUco markers and IR-trackers

B. Phantom Marking

Based on the results of the trajectory generation, we selected CPP for further investigation since it resulted in a higher TPR, a slightly lower FDR, and a lower variance. However, we can expect the results of the execution to be translatable to arbitrary surface trajectories, regardless of the projection method. Since the gelatine phantom melts under electrosurgery, we tested the phantom marking on a dummy device. Rather than applying actual power and measuring the power-out-ratio, we integrated a capacitive touch sensor that generates a binary signal (touch / no touch) comparable to the thresholded power output signal of the ESU. We further covered the top surface of the US phantom with a Low Density Polyethylene (LDPE) film to prevent the probe from poking through the surface. This also allowed us to repeat the execution several times without altering the phantom surface. We coated the LDPE film with US gel to produce a clearer change in the capacitive signal.

Similarly, for the surface trajectories generated from the US scans, we compare the overlap between the executed circular trajectory and the IMU-generated trajectory, using the calculated ground truth normal plane for projection.

To calculate the overlap between the executed and the inferred or ground truth trajectory, we downsampled the execution trajectory to only the points where the probe is initiating contact with the tissue surface. This resulted in a roughly

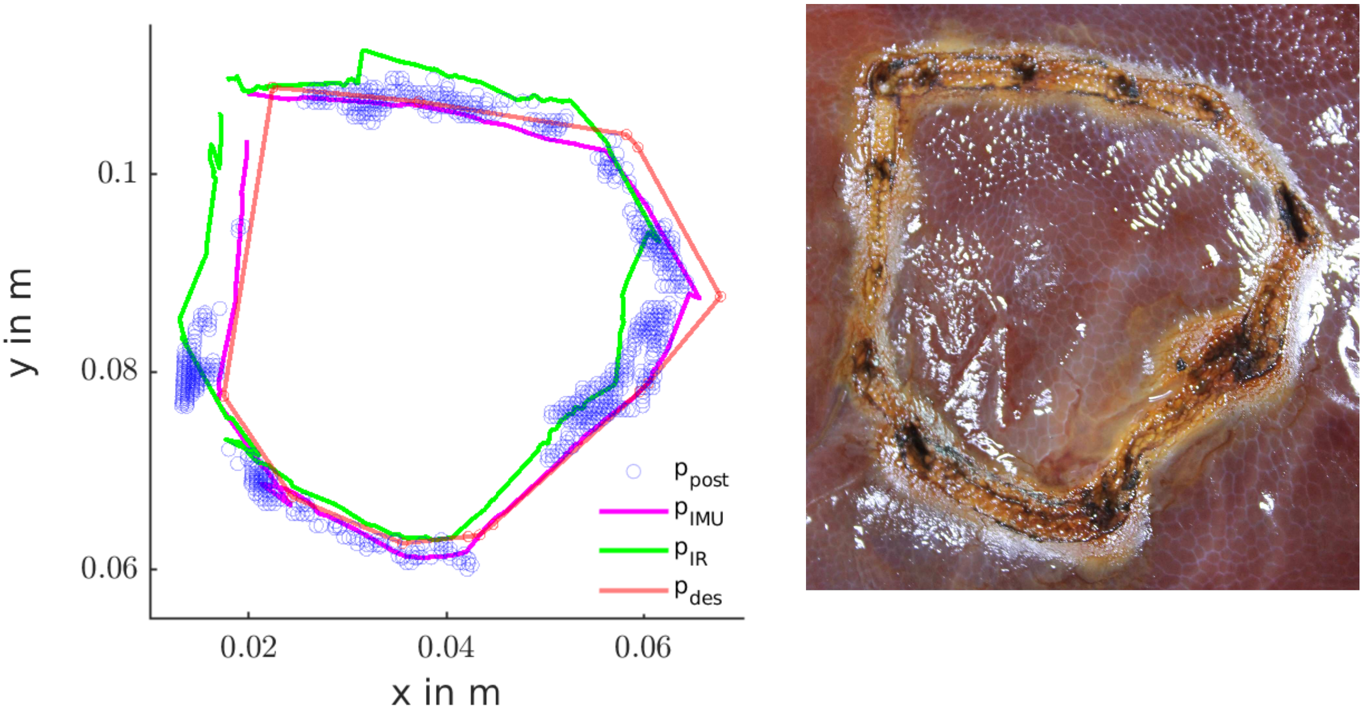

Fig. 11: Left: Projected ex-vivo results including point set obtained from the surface point scan. Right: Marked profile on the liver surface

$3-5mm$ spacing and ensured the trajectory points lay on the surface.

The controller provided good tracking with a mean error norm and mean error norm variation of $0.54 \pm 0.30mm$ and $0.7 \pm 0.53^\circ$ between the desired and executed IMU trajectory over all 15 runs and for position and orientation, respectively.

Overall, we found the mean positional error between the projected trajectories for ground truth (IR) and IMU to be $3.4 \pm 0.7mm$. This resulted in an overlap (TPR) of 0.875 ± 0.035 with the inferred area. FDR was found to be 0.135 ± 0.058. Both values are similar to the ones found for the 3D projection. Figure 9 shows exemplary results of an executed marking.

V. Ex-Vivo Feasibility Test

To assess the approach under more realistic conditions and to test the proposed control scheme with an actual ESU, we performed both previously tested routines on an ex-vivo porcine liver. In preparation, we cut a small pocket into the side of the liver, through which we inserted a hydrated PAM bead, representing a dummy tumor mass. The mass had similar dimensions (around $15mm$ diameter) to the ones previously used for the phantom study.

Similar to the phantom, we co-registered the IR tracking system as well as the stereo camera using spatial landmarks and ArUco markers. Figure 10 shows the setup for the ex-vivo trials, consisting of a polymer box for liquid retention and contamination prevention. Inside the box, we fixed a laser-cut frame holding the 3D-printed platform that contained all the necessary spatial landmarks to co-register PSM, stereo camera and IR tracking. On the bottom of the container, we placed the ground electrode of the ESU, covered with folded cloths soaked in saline, with sufficient osmolarity to match the required electrical impedance for the ESUs safety mechanism. In addition to electrical conductance and impedance matching, the cloth ensured sufficient friction to prevent the liver from slipping during scanning and marking.

At first, we scanned the liver with the stereo camera. To ensure that we caught the QR markers and the whole liver, we adjusted the distance between the camera and surface to $165mm$, slightly further than for the phantom, giving a more robust reconstruction of the surface structure and considerably less noise. We attribute this to the fact that the phantom surface contains more fine features than the relatively shiny and structureless gelatine surface. Additionally, this allowed us to decrease the point cloud grid size to $1mm$.

Equivalent to the phantom study, we placed the probe at a random location around the tumor with the US image plane normal pointing towards the phantom. After performing the scans, we calculated the projection; again choosing CPP. Lastly, we completed the execution of the marking onto the surface of the liver. For further validation, we used the 3D camera to scan the liver surface again. Using black ink, we dyed the trajectories. Figure 11 shows the color thresholded point set markered as blue dots p_{post}. This allowed us to perform colour thresholding on the 3D point cloud to extract the marked path directly from the surface scan. Aside from

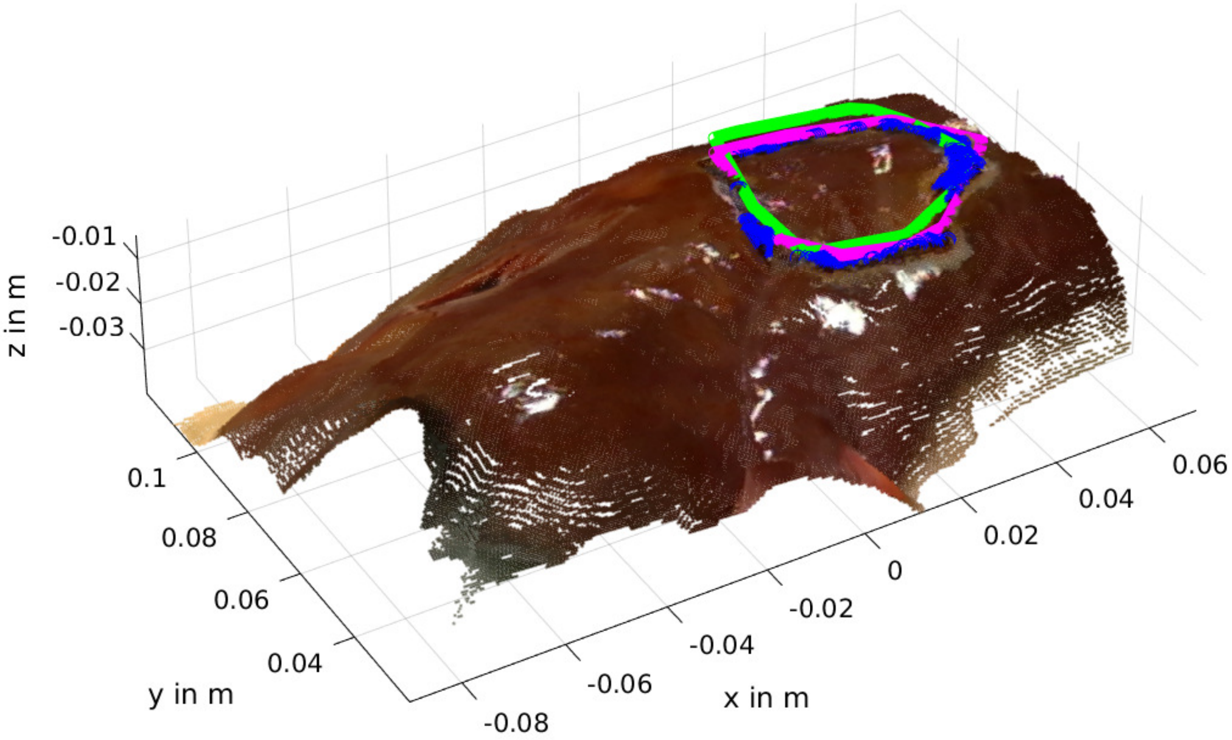

Fig. 12: 3D point cloud of ex-vivo liver, overlayed with the different trajectories corresponding to Figure 11

the previously employed kinematic data, this gave us a further means to assess the system's accuracy under these conditions.

Assessing the scan projection before execution, we found the TPR to be 0.844 and the FDR to be 0.119, comparable to those observed in the phantom study. Note, however, that as opposed to the phantom study, both projections were referenced against the same point cloud, as no ground truth point cloud was available.

Looking at the execution, we determined the TPR to be 0.905 and the FDR to be 0.130 when compared against the control input trajectory. Similarly, the TPR compared to the ground truth trajectory was 0.863, with an FDR of 0.133.

Figure 11 shows the results of the marking. We measured the width of the marking to be around $4mm$. The points at which the impedance adjustment occurred are clearly visible, marked by slight carbonisation and a deeper insertion into the tissue. The rest of the mark looks relatively even.

Looking at the extracted trajectories, we can see a relatively good match with the planned and executed trajectories (see Figure 11). Figure 12 further shows the overlay of these trajectories in 3D space. Looking at the IR-tracked trajectories, we find a TPR of 0.905 and an FDR of 0.129 for this single run, when compared to the input trajectory.

The distance between the two points in the cloud is $6.1mm$. This is significantly higher than the results of the tumor study. We believe a major reason for this may be the more flexible structure of the ex-vivo tissue, along with the more difficult segmentation of the US images.

VI. DISCUSSION AND CONCLUSIONS

We provided a novel approach for automating the marking of the resection margin on the tissue surface via electrocautery, including the integration of IMUs into US probe and a pick-up marking tool. We successfully demonstrated the feasibility and effectiveness of our approach in automating the marking of tumor boundaries on an organ surface in a controlled lab setting including an in-depth assessment of marking path planning and execution. Additionally, we sucessfully demonstrated the feasibility the approach onto an ex-vivo porcine liver sample.

While we were able to reduce the error to a range of several millimeters, this still had a noticeable effect on the results of the scanning and marking. We value the achieved TPR between 0.8 and 0.9 and FDR between 0.05 and 0.15 as a success and a potential benchmark for future attempts to automate tumor margin marking. The quantified positional accuracy of around $3mm$ needs to be further improved to ensure reliability, an increase in TPR and decrease in FDR. It should also be noted that the $3mm$ error is relatively close to the roughly $15mm$ mass size. Employing the system for larger masses will consequently increase the TPR, and decrease the FDR and increase the likelihood of reaching an acceptable reliability level. While there is a maximum tumor size that can be considered for laparoscopic resection, it may still be useful for certain pathologies. It should further be noted that in its current state the system may only be employed on convex tumors, although an extension should be implementable through more complex methods such as using concave instead of convex sets.

Further improvements should also be made to reduce carbonization and the thickness of the marking. As a first step, a smaller marking tip could be used. This, however, will most likely also influence the contact surface and thus the power transfer. A more generic solution would be to investigate a more fine-grained method to measure impedance and thus the contact quality. Being a feasibility study, an optimisation of the contact control and detection for the electrosurgery tool are out of scope. Improving it would require further insights into the workings of the controller or more precise measurements of the contact impedance. This could include a more thorough characterisation of the power output over different surface impedances, a modification of the ESU, or a further opening of the data interface by the manufacturer.

Future work will be focused on further increasing the accuracy of the system. Currently, this is mainly limited by the robot's positional accuracy as well as the point cloud obtained through the camera. Additionally, we intend to transition towards a more practical solution for hand-eye calibration, as ArUco markers are not well suited to be employed within the abdomen as outlined in Section III-D. With these challenges solved, we intend to assess the system in an even more realistic cadaveric or animal studies. For the latter, further approaches would need to be investigated to account for breathing and heart beat motion that have been ignored for the scope of this work. Another possibility could be to account for uncertainty along the pipeline and integrate this into the calculation and even the outlining of the margined tumor projection [39]. Additionally, an improved 3D reconstruction of the tumor may be achieveable by following approaches for fusing IMU signals and US images as investigated in [41] for freehand scans.

In terms of medical applications, it would be interesting to extend the approach to marking further anatomical boundaries, such as the resection lines along segments. Additionally, more elaborate methods for calculating the projection on the surface are possible, in particular methods that reduce the resection volume in a more discriminate manner. It could also be interesting to investigate performing full resections of tumors or organ segments. Furthermore, we could see the markings to be used for AR projections to give the surgeon a clearer image of where the tumor lies with respect to the outlined projection.

Future work should also include moving away from ArUco markers and towards a more practical solution. One promising direction may be to use instrument surface registration, as previously explored in [40].

APPENDIX

VII. US PHANTOM COMPOSITION

TABLE II: Ingredients for US phantom

Ingredient	Function	Mass Ratio
DI Water	Tissue mimicking base structure	67.7%
Gelatin	Tissue mimicking base structure	22.5%
Glycerol	Flexibility	9.7%
Flour	Scattering	0.1%

VIII. NOMENCLATURE

In general we use **bold** variables to denote vectors and normal *italic* variables to denote single value variables.

A. Point Sets

We use curved brackets to denote point sets e.g. $\{A\}$, such as the convex hull. To denote individual points within this set we use $\mathbf{p}_i^{(A)}$. Additional subscription may be used to further denote the set such as $\{A_{CV}\}$ and $\mathbf{p}_i^{(A_{CV})}$, to denote a convex hull set.

B. Transformations

Transformations with just a single subscript such as $\mathbf{T}_A$ (including R_A and $\mathbf{p}_A$) are used to refer to the coordinate frames themselves, while the transformation from a coordinate frame $\mathbf{T}_B$ to coordinate frame $\mathbf{T}_A$, e.g. transforming a point expressed in $\mathbf{T}_B$ coordinates into $\mathbf{T}_A$, is written as $\mathbf{T}_A^B$ and denoted with subscript and superscript. Further superscripts may be added $\mathbf{T}_A^{B,des}$ to specify frames more accurately, in this case the desired (abbreviated as des) relative pose of B with respect to A. $\mathbf{T}_A^B$ defines a homogeneous transformation, combining a rotation $\mathbf{R}_A^B$ and a translation $\mathbf{p}_A^B$

$$T_A^B = \begin{bmatrix} \mathbf{R}_A^B & \mathbf{p}_A^B \\ 0\ 0\ 0 & 1 \end{bmatrix} \tag{18}$$

For vectors, we use uppercase letters for the superscript to denote defined coordinate frame quantities (e.g., relative position of the origin $\mathbf{p}_A^B$ or coordinate axes $\mathbf{x}_A^B$, $\mathbf{y}_A^B$ and $\mathbf{z}_A^B$). We further use lowercase letters to specify relative positions without defined coordinate frames. The only exception is the gravity vector $\mathbf{g}_A$, which does not specify a reference frame or lowercase subscript, as gravity is a world-implicit quantity (e.g., implying a specific orientation).

C. Kinematic Notation

We denote robotic end-effector poses, composed of translation $\mathbf{p}$ and rotation θ roll, pitch and yaw angle as

$$\mathbf{x} = \left[p_x, p_y, p_z, \theta_r, \theta_p, \theta_y\right] \tag{19}$$

Equivalently, in joint space, we express the set of six joint angles θ as

$$\theta = \left[\theta_{l1}, \theta_{l2}, q_{l3}, \theta_{l4}, \theta_{l5}, \theta_{l6}\right] \tag{20}$$

the ultimate joint angle (q_{l7}), corresponding to the jaw opening, is excluded as it describes a separate separate degree of freedom.

The forward kinematics solution can be calculated by multiplying the parameterised transformations from the base of the robots until the tooltip (e.g., following the Denavit-Hartenberg convention).

$$\mathbf{x} = \mathbf{f}(\theta) \tag{21}$$

Inverse Kinematics are the inverse of forward kinematics, defined as

$$\mathbf{q} = \mathbf{f}^{-1}(\mathbf{x}) \tag{22}$$

Note that the solution to this equation is generally not guaranteed to exist in symbolic form. A general approach is to approximate the solution numerically. In this work, the inverse solution is provided by the dVRK software framework.

IX. PLANAR PROJECTIONS

For the projection of an arbitrary point $\mathbf{x}_a$ via an arbitrary unit vector $\mathbf{v}_a$ into a plane defined by point $\mathbf{x}_p$ and normal vector $\mathbf{n}_p$ the following equation must hold

$$\mathbf{n}_p^T \cdot (\mathbf{x}_a - \underbrace{(\mathbf{x}_p + \sigma \mathbf{v}_a)}_{\mathbf{x}_{a,proj}}) = 0 \tag{23}$$

Solving for σ and plugging the result into the definition of $\mathbf{x}_{a,proj}$ leads to the following result

$$\mathbf{x}_{a,proj} = \mathbf{x}_p + \underbrace{\left(\frac{\mathbf{n}_p^T \cdot (\mathbf{x}_p - \mathbf{x}_a)}{\mathbf{n}_a^T \cdot \mathbf{v}_a}\right)}_{\sigma} \mathbf{n}_p \tag{24}$$

Note that in the particular case of $\mathbf{v}_a$ being the normal vector, $\mathbf{n}_p^T \cdot \mathbf{n}_p = 1$ reduces the denominator leading to

$$\mathbf{x}_{a,proj} = \mathbf{x}_p + \underbrace{(\mathbf{n}_p^T \cdot (\mathbf{x}_p - \mathbf{x}_a))}_{\sigma} \mathbf{n}_p \tag{25}$$

REFERENCES

[1] E. J. Hagpian ”Liver Ultrasound: A key procedure in the surgeon’s toolbox,” Journal of Surgical Oncology vol. 122, no. 1, pp. 61-69, Mar. 2020.

[2] M. Makuuchi, H. Hasegawa and S. Yamazaki, ”Ultrasonically guided subsegmentectomy,” Surgery, Gynecology & Obstetrics, vol. 161, no. 4, pp. 346-350, Oct. 1985.

[3] M. Makuuchi, ”Surgical treatment for HCC–special reference to anatomical resection,” International Journal of Surgery, Vol. 11, Suppl. 1, pp.S47-S49, Dec. 2013.

[4] S. Dietsch, L. Lindenroth, A. Stilli and D. Stoyanov (2023). ”Imaging skins: Stretchable and conformable on-organ beta particle detectors for radioguided surgery,” Progress in Biomedical Engineering, Vol. 5, no. 3, pp. Jun 2023.

[5] J. Liu, G. Singh, S. Al’Aref, B. Lee, O. Oleru, J.K. Min et al., ”Image registration in medical robotics and intelligent systems: fundamentals and applications.” Advanced Intelligent Systems, Vol. 1, no. 6, 2019.

[6] F. Taquee, O. Goksel, S. S. Mahdavi, M. Keyes, W. J. Morris, I. Spadinger and S. Salcudean, ”Deformable prostate registration from MR and TRUS images using surface error driven FEM models,” in Medical Imaging 2012: Image-Guided Procedures, Robotic Interventions, and Modeling, Vol. 8316, D. R. Holmes III and K. H. Wong, Eds. Bellingham, WA, USA: SPIE, 2012, pp. 335-344.

[7] O. Heizmann, S, Zidowitz, H. Bourquain, S. Potthast, H.-O. Peitgen, D. Oertli and C. Kettelhack, ”Assessment of intra-operative liver deformation during hepatic resection: prospective clinical study,” World Journal of Surgery, Vol. 34, no. 8, pp. 1887-1893, Aug. 2010.

[8] W. Wein, A. Ladikos, B. Fuerst, A. Shah, K. Sharma, N. Navab, ”Global Registration of Ultrasound to MRI Using the LC2 Metric for Enabling Neurosurgical Guidance.”, In: Mori, K., Sakuma, I., Sato, Y., Barillot, C., Navab, N. (eds) Medical Image Computing and Computer-Assisted Intervention – MICCAI 2013. MICCAI 2013. Lecture Notes in Computer Science, vol 8149. Springer, Berlin, Heidelberg.

[9] X. Huang, ,J. Moore, G. Guiraudon, D.L. Jones, D. Bainbridge. J. Ren and T.M. Peters, ”Dynamic 2D Ultrasound and 3D CT Image Registration of the Beating Heart,” IEEE Transactions on Medical Imaging, Vol. 28, no. 8, 2009.

[10] N. Golse, A. Petit, M. Lewin, E. Vibert and S. Cotin, ”Augmented reality during open liver surgery using a markerless non-rigid registration system,” Journal of Gastrointestinal Surgery, Vol. 25, no. 3, pp. 662-671, Mar. 2021.

[11] P. Mathur, G. Samei, K. Tsang, J. Lobo and S. Salcudean, ”On the feasibility of transperineal 3D ultrasound image guidance for robotic radical prostatectomy,” International Journal of Computer Assisted Radiology and Surgery, Vol. 14, no. 6, pp. 923-931, Jun. 2019.

[12] Z. Jiang, S.E. Salcudean and N. Navab, ”Robotic ultrasound imaging: State-of-the-art and future perspectives,” Medical Image Analysis, Vol. 89, July 2023.

[13] O. Mohareri, M. Ramezani, T. Adebar, P. Abolmaesumi and S. Salcudean, ”Automatic detection and localization of da Vinci tool tips in 3D Ultrasound,” in Information Processing in Computer-Assisted Interventions, P. Abolmaesumi, L. Joskowicz, N. Navab and P. Jannin, Eds. Heidelberg, Germany: Springer International Publishing, 2012, pp. 22-32.

[14] C. Schneider, J. Guerrero, C. Nguan, R. Rohling and S. Salcudean, ”Intra-operative ”pick-up” ultrasound for robot assisted surgery with vessel extraction and registration: a feasibility study,” in Information Processing in Computer-Assisted Interventions, R.H. Taylor and G.-Z. Yang, Eds. Heidelberg, Germany: Springer International Publishing, 2011, pp. 122-132.

[15] A. Attanasio, B. Scaglioni, E. De Momi, P. Fiorini, P. Valdastri, ”Autonomy in Surgical Robotics,” Annual Review of Control, Robotics, and Autonomous Systems, Vol. 4, no. 1, pp.651-679, May 2021.

[16] J. Leven, D. Burschka, R. Kumar, G. Zhang, S. Blumenkranz, X. Dai, M. Awad et al. ”DaVinci canvas: a telerobotic surgical system with integrated, robot-assisted, laparoscopic ultrasound capability,” in Medical Image Computing and Computer-Assisted Intervention – MICCAI 2005, Part I, : J.S. Duncan and G. Gerig, Eds. Heidelberg, Germany: Springer International Publishing, 2005, pp. 811-818.

[17] N. Marahrens, B. Scaglioni, D. Jones, R. Prasad, C.S. Biyani and P. Valdastri, ”Towards Autonomous Robotic Minimally Invasive Ultrasound Scanning and Vessel Reconstruction on Non-Planar Surfaces”, Frontiers in Robotics and AI, Vol. 9, Art. 940062.

[18] J.M. Ferguson, B. Pitt, A. Kuntz, J. Granna, N.L. Kavoussi, N. Nimmagadda, E.J. Barth, S.D. Herrell III and R.J. Webster III, ”Comparing the accuracy of the da Vinci Xi and da Vinci Si for image guidance and automation,” The International Journal of Medical Robotics and Computer Assisted Surgery, Vol. 16. no. 6 pp. 1-10, 2020.

[19] B. Thananjeyan, A. Garg, S. Krishnan, C. Chen, L. Miller and K. Goldberg, ”Multilateral surgical pattern cutting in 2d orthotropic gauze with deep reinforcement learning policies for tensioning,” 2017 IEEE international conference on robotics and automation (ICRA), Singapore, Singapore, pp. 2371-2378, 2017.

[20] S. Mckinley, A. Garg, S. Sen, D.V. Gealy, J.P. Mckinley, Y. Jen and K. Goldberg, ”An interchangeable surgical instrument system with application to supervised automation of multilateral tumor resection,” 2016 IEEE International Conference on Automation Science and Engineering (CASE), Fort Worth, TX, USA, 2016, pp. 821-826.

[21] H. Saeidi, J.D. Opfermann, M. Kam, S. Wei, S. Leonard, M.H. Hsieh, J.U. Kang and A. Krieger, ”Autonomous robotic laparoscopic surgery for intestinal anastomosis,” Science Robotics Vol. 7, no. 62, 2022.

[22] J.D. Opfermann, Ss Leonard, R.S. Decker, N.A. Uebele, C.E. Bayne, A.S. Joshi and A. Krieger, ”Semi-autonomous electrosurgery for tumor resection using a multi-degree of freedom electrosurgical tool and visual servoing,” 2017 IEEE/RSJ International Conference on Intelligent Robots and Systems (IROS), Vancouver, BC, Canada, 2017, pp. 3653-3660.

[23] H. Saeidi, J. Ge, M. Kam, J.D. Opfermann, S. Leonard, A.S. Joshi, and A. Krieger. ”Supervised autonomous electrosurgery via biocompatible near-infrared tissue tracking techniques,” IEEE transactions on medical robotics and bionics, Vol. 1, no. 4 pp. 228-236, 2019.

[24] P. Pratt, A. Hughes-Hallett, L. Zhang, Nisha Patel, E. Mayer, Ara Darzi and G.-Z. Yang, ”Autonomous ultrasound-guided tissue dissection,” in Medical Image Computing and Computer-Assisted Intervention - MICCAI 2015, Part I, N. Navab, J. Hornegger, W.M. Wells and A. Frangi, Eds. Heidelberg, Germany: Springer International Publishing, 2015, pp. 249-257.

[25] C. D'Ettorre, A. Mariani, A. Stilli et al. ”Accelerating surgical robotics research: A review of 10 years with the da vinci research kit” IEEE Robotics & Automation Magazine, Vol. 28, no. 4, pp. 56-78, Deb. 2021.

[26] Z. Cui, J. Cartucho and S. Giannarou, ”Caveats on the first-generation da Vinci Research Kit: latent technical constraints and essential calibrations,” arXiv:2210.13598.

[27] A. Avinash, A. E. Abdelaal, P. Mathur, and S. E. Salcudean. ”A” pickup” stereoscopic camera with visual-motor aligned control for the da Vinci surgical system: a preliminary study,” International Journal of Computer Assisted Radiology and Surgery, vol. 14, no. 7 pp. 1197-1206., 2019.

[28] R. Mahony, T. Hamel, P. Morin and E. Malis, ”Nonlinear complementary filters on the special linear group,” IEEE Transactions on Automatic Control, vol. 53, pp. 1203–1218, 2008.

[29] https://github.com/jhu-dvrk/sawIntuitiveResearchKit/wiki/SUJ, accessed: 13/07/2023

[30] D.M. Kwartowitz, M.I. Miga, S.D. Herrell and R.L. Galloway, ”Towards image guided robotic surgery: Multi-arm tracking through hybrid localization,” International Journal of Computer Assisted Radiology and Surgery, vol. 4, no. 3, pp. 281–286, 2009.

[31] A. Attanasio, B. Scaglioni, M. Leonetti, A.F. Frangi, W. Cross, C.S. Biyani and P. Valdastri, ”Autonomous tissue retraction in robotic assisted minimally invasive surgery – a feasibility study,” IEEE Robotics and Automation Letters, vol. 5, no. 4, pp.6528-6535, 2020.

[32] Z. Cheng, D. Dall'Alba, K.L. Schwaner, P. Fiorini and T.R. Savarimuthu, ”Robot assisted electrical impedance scanning for tissue bioimpedance spectroscopy measurement,” Measurement, Volume 195, May 2022.

[33] O. Ronneberger, P. Fischer and T. Brox, ”U-Net: Convolutional Networks for Biomedical Image Segmentation,” in Medical Image Computing and Computer-Assisted Intervention – MICCAI 2015. MICCAI 2015, N. Navab, J. Hornegger, W. Wells and A. Frangi, eds. Heidelberg, Germany: Springer International Publishing, 2015.

[34] C.B. Barber, D.P. Dobkin and H. Huhdanpaa ”The quickhull algorithm for convex hulls,” ACM Transactions on Mathematical Software, vol. 22, no. 4, pp.469–483, 1996.

[35] T. J. Vogl, N.E.A. Nour-Eldin, R.M. Hammerstingl, B. Panahi and N.N. Naguib, ”Microwave ablation (MWA): basics, technique and results in primary and metastatic liver neoplasms–review article,” RöFo - Fortschritte auf dem Gebiet der Röntgenstrahlen und der bildgebenden Verfahren, vol. 189, no. 11, pp. 1055-1066, Nov. 2017.

[36] B. Chen, S. Shen, J. Wu, Y. HuaY., Kuang, M., Li, S., and B. Peng, ”CISD2 associated with proliferation indicates negative prognosis in patients with hepatocellular carcinoma.” International journal of clinical and experimental pathology, vol. 8 no. 10, 2015.

[37] L. Liu, R. Miao, H. Yang, X. Lu, Y. Zhao, Y. Mao et al., ”Prognostic factors after liver resection for hepatocellular carcinoma: a single-center experience from China.” The American journal of surgery, Vol. 203, no. 6, 2012.

[38] Z. Hamad, I.C. Cameron, J. Wyatt, R.K. Prasad, G.J. Toogood and J.P.A. Lodge, ”Resection margin in patients undergoing hepatectomy for colorectal liver metastasis: a critical appraisal of the 1 cm rule.” European Journal of Surgical Oncology (EJSO), Vol. 32, no. 5, 2006.

[39] M. Siebold, J. Ferguson, B. Pitt; N. Kavoussi, N. Nimmagadda, D. Herrell and R.J. Webster III, ”Choosing Statistically Safe, Variable-Thickness Margins in Robot-Assisted Partial Nephrectomy,” 2020 International Symposium on Medical Robotics (ISMR), Atlanta, GA, USA, 2020, pp. 152-158.

[40] J.M. Ferguson, L.Y. Cai, A. Reed, M. Siebold, S. De, S. D. Herrell and R.J. Webster III, ”Toward image-guided partial nephrectomy with the da Vinci robot: exploring surface acquisition methods for intra-operative re-registration,” in Medical imaging 2018: Image-guided procedures, robotic interventions, and modeling, vol. 10576, B. Fei, R.J. Webster III, Eds. Bellingham, WA, USA: SPIE, 2018, pp. 335-344.

[41] R. Prevost, M. Salehi, J. Sprung, A. Ladikos, R. Bauer and W. Wein, ”Deep learning for sensorless 3D freehand ultrasound imaging. In International conference on medical image computing and computer-assisted intervention.”, International conference on medical image computing and computer-assisted intervention, Cham: Springer International Publishing, 2017, pp. 628-636.

Nils Marahrens holds an M.Sc. in Mechanical Engineering ('17) as well as a B.Sc. in Engineering Science ('14) from the Technical University of Munich (TUM) and is currently a final year PhD student at STORM Lab, University of Leeds, focusing on autonomous surgical assistance via ultrasound. Previously, Nils also worked as an engineering research associate at the University Hospital Rechts der Isar of TUM, contributing to the areas of surgical data science and robotically assisted laparoscopy.

Dominic Jones (Member, IEEE) received the M.Eng degree in Mechanical Engineering, the Ph.D. degree in Medical Mechatronics in 2015 and 2019, respectively. He is currently a Lecturer (Assistant Professor) with the University of Leeds, Leeds, U.K. His research interests include autonomy in surgical robotics, tactile sensing in surgical tools, and skill assessment in surgical training.

Nikita Murasovs Nikita Murasovs finished his B.Eng at the University of Aberdeen. Currently, he is pursuing a PhD in the area of surgical robotics under the supervision of Prof. Pietro Valdastri at the University of Leeds.

Chandra Shekhar Biyani is a Consultant Urological Surgeon at St. James's University Hospital, Leeds. He has developed expertise in stone disease and laparoscopy. Mr. Biyani trained in General Surgery in India and Urology training in the UK. He is a keen surgical trainer and has delivered courses in UK, Africa and Europe. He received a Special Recognition Award at the Zenith Global Health Awards 2019 for his work in Africa. He was instrumental in developing National Urology Simulation Boot Camp for new urology registrars. He was awarded the John Anderson Medal for his educational activities by the British Association of Urological Surgeons in 2022. He is also Co-Lead for the Cadaveric Simulation Centre (CADSIM) at the University of Leeds. He has been awarded a British Empire Medal for his work in medical education.

Pietro Valdastri (M'05, SM'13) received a Master's (Hons., Univ. Pisa, 2002) and Ph.D. (Biomed. Eng, SSSA, 2006). He is Professor and Chair in robotics and autonomous systems at University of Leeds. His research interests include robotic surgery, robotic endoscopy, design of magnetic mechanisms and medical capsule robots. Prof. Valdastri is the recipient of the Wolfson Research Merit Award from the Royal Society.